Title

High-performance organic photodetectors enabled by a refined fibrillar multiphase morphology

Authors

Quan, Huilei

Zhong, Zhiming

Hao, Tianyu

et al.

Publication Date

2023

DOI

10.1016/j.cej.2022.139295

High-performance organic photodetectors enabled by a refined fibrillar multiphase morphology

Huilei Quan [a,d], Zhiming Zhong [a,d], Tianyu Hao [b], Kang An [a,d], Wenkai Zhong [b,*], Cheng Wang [c], Feng Liu [b], Lei Ying [a,d,*], Fei Huang [a,d,*]

[a] *Institute of Polymer Optoelectronic Materials and Devices, State Key Laboratory of Luminescent Materials and Devices, South China University of Technology, Guangzhou 510640, China*

[b] *Frontiers Science Center for Transformative Molecules, Center of Hydrogen Science, and School of Chemistry and Chemical Engineering, Shanghai Jiao Tong University, Shanghai 200240, China*

[c] *Advanced Light Source, Lawrence Berkeley National Laboratory, Berkeley, CA 94720, USA*

[d] *South China Institute of Collaborative Innovation, Dongguan 523808, China*

*Corresponding authors:

E-mail addresses: zhongwk@sjtu.edu.cn (W. Zhong); msleiying@scut.edu.cn (L. Ying); msfhuang@scut.edu.cn (F. Huang)

ABSTRACT

Film morphology of donor:acceptor blend layers play a critical role in photon-to-current efficiency and dark/noise current of organic photodetectors (OPDs). One effective approach to manipulate crystallization and mesoscale phase separation of such blend layers is sequential casting (SC). However, the guiding strategies to control the morphology and the impacts on OPD performances of the SC films remain elusive, as the film structural evolution during SC is different from conventional blend casting (BC). Here, a refined fibrillar multiphase morphology is demonstrated by SC in an NT812:IEICO-4F blend film, where the high-quality IEICO-4F crystallites infiltrate the robust NT812 fibril network from the surface to the bulk. Such a morphology leads to improved charge generation and collection, reduced trap states, and enhanced charge block capability of resultant device, enabling simultaneous achievement of high external quantum efficiency and low dark/noise current. A maximum special detectivity of 5×10^{13} Jones is achieved at 860 nm under –0.1 V, which is among the highest detectivities for vis-to-NIR OPDs. The linear dynamic range and response speed are also improved. Such enhancements are parallelly observed from OPD devices based on other blend systems with similar fibrillar refinement, which provides guidelines for film structure manipulation towards high OPD performances.

Keywords:

Sequential casting; Film morphology; Density of trap state; Organic photodetector

1. Introduction

Organic photodetectors (OPDs) present great advantages of cost-efficient film processing, tunable spectral response, and ease to be light-weight and flexible, which arouse broad interests from academia and industry for multiple sensing applications [1-5]. Recent OPD research concerns how to improve the light-sensing performances with spectral response extended from the visible (vis) region to the near-infrared (NIR) region, amid the emergence of narrow bandgap non-fullerene acceptors (NFAs) [6-12]. Similar to organic photovoltaics, the active layer in an OPD device is generally prepared by blend casting (BC) the donor:acceptor (D:A) mixed solution, which results in a bulk heterojunction (BHJ) structure associated with bi-continuous phase separation [13,14]. Such a BHJ structure brings success in realizing high external quantum efficiency (EQE) of device spanning multiple D:A blend systems, as charge carrier generation and collection are optimized [15-17]. However, it is inevitable that BC approach would lead to direct contacts of acceptor with the anode and donor with the cathode, which could increase charge injection from the electrodes to active layer under reverse bias, and thus, increasing the dark/noise current of OPD devices. Notably, this phenomenon will be exacerbated in the blend systems based on narrow bandgap NFAs, due to their smaller electron injection barriers [18,19]. Therefore, it is fundamentally challenging to simultaneously achieve high EQE and low dark/noise current of OPDs by optimizing morphology of the active layer [20-22].

To tackle such challenge, multiple effective strategies have been employed, such as increase of film thickness [18], construction of ternary blends [23], incorporation of an interlayer [24,25], and use of sequential casting (SC) [26-29]. Among these, SC can generate a blend film with a gradient component distribution in vertical direction, which is carried out by casting the acceptor (or donor) atop the pre-deposited donor (or acceptor) layer. Considering the processing solvent for the upper layer will erode or swell the underneath layer during the deposition process, it is rational to anticipate that the interface between the two layers is in the form of BHJ structure. The resultant vertical component distribution is essentially favorable for blocking charge injection under reversed bias, and hence, decreasing the dark/noise current. Meanwhile, SC is found to modulate the material crystallization and phase separation, which can well facilitate the exciton dissociation and charge transport [30-32]. Therefore, the SC devices are potential to exhibit high EQE and low dark/noise current simultaneously, as well as significantly improved OPD performances. Despite these assets, the guiding strategies for morphology manipulation of OPD thin-films remain elusive, and need to be explored for further boosting the performances.

In this work, SC is employed to fabricate the OPD blend film consisting a D:A combination of NT812:IEICO-4F, where the IEICO-4F is spin-casted on the top of the pre-deposited NT812 layer. The resultant SC film shows a refined fibrillar multiphase morphology, where the high-quality IEICO-4F crystallites infiltrate the NT812 fibril network from the surface to the bulk. The combination of improved charge generation and collection, reduced trap states, and vertical component distribution enables the

simultaneous achievement of enhanced EQE and reduced dark/noise current. Efficient vis-to-NIR sensing performances are realized, with a maximum special detectivity (D^*) of 5×10^{13} Jones at 860 nm under a reversed bias of –0.1 V and a linear dynamic range of 129 dB. The D^* of the SC device is three times higher than the BC device with 1.5×10^{13} Jones. Performance improvements are parallelly obtained from other D:A combinations with similar morphology, indicating that the SC-induced refined fibrillar multiphase morphology can realize new opportunities for developing high-performance OPDs.

2. Results and discussion

2.1 Materials and device performance

The chemical structures, energy levels, and absorption spectra of NT812 and IEICO-4F are shown in Figs. 1a-c. The staggered alignment of lowest unoccupied molecular orbital (LUMO) and highest occupied molecular orbital (HOMO) energy levels of NT812 and IEICO-4F is beneficial to charge separation when the photogenerated excitons reach the D/A interface [33-36]. The NT812:IEICO-4F blend film shows a broad absorption profile ranging from 300 to 1000 nm, indicating the photon-harvesting capability of the blend films across the vis-to-NIR region. It is seen that the absorbance contribution from IEICO-4F (peak at ~850 nm) is increased in the SC film compared with the BC film, which is favorable for increasing NIR sensing of the OPD device. The film processing methods are schematically shown in Fig. 1d. For BC, the blend film is spin-casted from chlorobenzene (CB) solution of NT812:IEICO-

4F mixture. For SC, the neat NT812 layer is pre-casted from CB solution, and the neat IEICO-4F chloroform (CF) solution is casted on the NT812 layer. The use of CB as the processing solvent for the NT812 layer can better promote the polymer crystallization compared with CF (Fig. S1). As NT812 can also be dissolved in CF, IEICO-4F would inevitably infiltrate NT812 from top to bottom of the film, forming interdiffusion of components in vertical direction. Such assumption can be verified by time-of-flight secondary ion mass spectrometry (TOF-SIMS) measurements of the films (Fig. S2). TOF-SIMS depth profiles were obtained by using F^- and SN^- signals as chemical labels to track the IEICO-4F and NT812, respectively. It can be seen that from top to bottom of the SC film, the ratio of IEICO-4F shows gradient decrease, while the ratio of NT812 shows gradient increase. For the BC film, both components show an average distribution over the thickness direction.

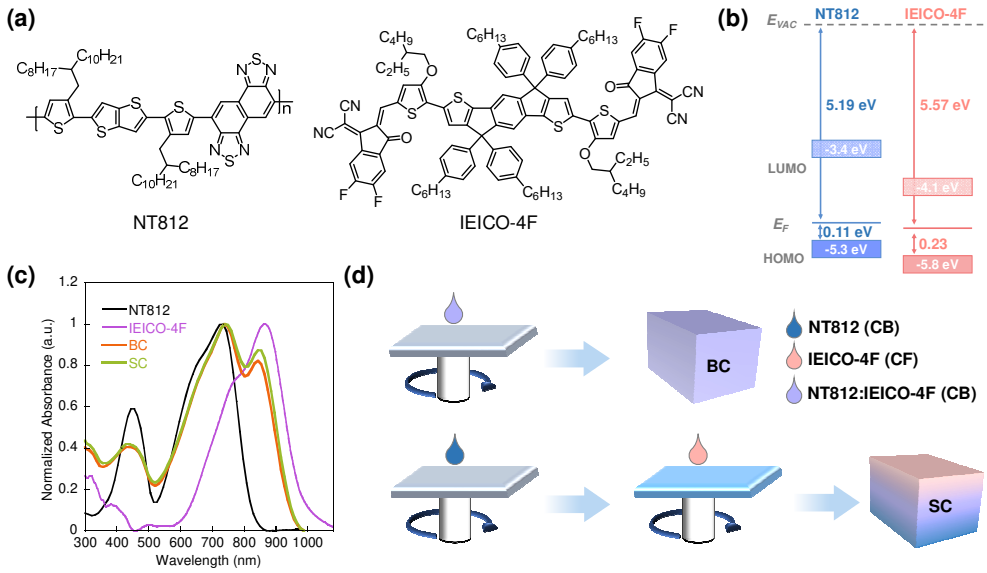

Fig. 1. (a) Chemical structures and (b) Energy levels of NT812 and IEICO-4F. (c) Absorption spectra of neat materials and blend films prepared by BC and SC. (d)

Schematic representations of the film processing approaches and vertical component distributions of the resultant films as estimated by TOF-SIMS measurements.

The OPD devices based on the BC and SC blends were fabricated with architecture of ITO/PEDOT:PSS (18 nm)/NT812:IEICO-4F/LiF (1 nm)/Al (70 nm). The thickness of the active layer was kept at ~300 nm. The thickness of the BC film was controlled by the spin rate of the solution. For the SC film, the thickness varied with the diffusion degree of the IEICO-4F into the NT812 layer, which can be controlled by the thickness of the NT812 or the processing solvent for the IEICO-4F. The diffusion degree of the IEICO-4F in SC film can also strongly influence the D:A ratio. Shown in Fig. S3a are the UV-vis absorption spectra of SC films with different thicknesses. It can be seen that the absorption peak at ~850 nm declines with film thickness increasing, as the NT812 layer with higher thickness can mitigate the diffusion of IEICO-4F, resulting lower IEICO-4F doping content in the film. The blend ratios of the SC films are estimated by comparing the absorption spectra of BC films with given blend ratios (Figs. S3b,c). Fig. S4 summarizes device performances of SC films with different thicknesses, and best performance was obtained under ~300 nm. We also changed the processing solvent of IEICO-4F with CB, but the resulting SC film shows low-quality film formation, leading to deteriorated device performances (Fig. S5).

The spectral response of devices at –0.1 V bias is shown in Fig. 2a. In comparison with the BC device, the SC device shows increased EQE from ~45% to ~60% over the wavelength range of 620-870 nm. The photo-responsivity (R) of

devices can be calculated by [37]:

$$R = \frac{J_{ph}}{L_{light}} = \frac{EQE \times \lambda}{1240}\ (\mathrm{A\ W^{-1}}) \quad (1)$$

where J_{ph} is the photocurrent, L_{light} is the incident light power, and λ is the wavelength of incident light in nanometer. Apparently, the increased EQE of SC device leads to enhanced responsivity of 0.42 A W^{-1} at 860 nm. Shown in Fig. 2b are the current density-voltage (*J*-*V*) curves of devices under dark condition. The SC device shows decreased dark current density (J_d) under reverse bias, which is beneficial for obtaining lower noise level and higher sensing capability to weak light signals. The J_d of the SC device is 2.2×10^{-10} A cm^{-2} under –0.1 V, which is one of the lowest values of reported OPDs [38 - 42]. To quantify the detection capability, the specific detectivities (D^*) are calculated following the equation [43,44]:

$$D^* = R \times \frac{\sqrt{A}}{S_n} = \frac{R}{\sqrt{2qJ_d}} = \frac{EQE \times \lambda}{1240} \times \frac{1}{\sqrt{2qJ_d}}\ (\mathrm{Hz^{1/2}\ W^{-1}\ or\ Jones}) \quad (2)$$

where A is device area, S_n is the noise power density, and q is the elementary charge [45]. The noise power density as a function of frequency at –0.1 V is shown in Fig. 2c. The SC device shows lower S_n values at the low-frequency region, which are more approaching the background noise, indicating less flicker noise compared with the BC device [46]. The *D** values at 860 nm derived from *R* and S_n (10 kHz) are of 4.7×10^{12} Jones and 9.5×10^{12} Jones for BC and SC devices, respectively. As the device noise is out of the detection limit of the instrument at high-frequency region, the *D** values calculated by this approach are underestimated. Following the abovementioned equation, the D^* can also be derived by the device EQE and J_d, and the calculated results are summarized in Fig. 2d. The SC device exhibits higher D^* values than those

of the BC device within the probed wavelength range, due to the increased EQE and reduced J_d. A maximum D^* of 5.0×10^{13} Jones is achieved at 860 nm, which is among the highest values for reported vis-to-NIR OPDs [47-51].

The linear dynamic range (LDR) was used to evaluate the range where the device output signals scale linearly with the input signals, since the devices need to detect the weak light and operate across a broad range of light intensity [52]. The LDR is calculated by

$$\mathrm{LDR} = 20\log\frac{J_{\mathrm{upper}}}{J_{\mathrm{lower}}} = 20\log\frac{I_{\mathrm{upper}}}{I_{\mathrm{lower}}}(\mathrm{dB}) \quad (3)$$

where J_{upper} (I_{upper}) and J_{lower} (I_{lower}) represent the highest and the lowest photocurrent density (light intensity), respectively, between which the input-output signal relation coincides with linearity. The light-intensity dependent *J-V* characteristics of the devices are plotted in Figs. S6a,b, and the photocurrent density (J_{ph}, $J_{ph} = J_L - J_d$) at –0.1 V as a function of light intensity is shown in Fig. 2e. The BC device has a linear response from 3.9×10^{-9} W cm^{-2} to 2.1×10^{-3} W cm^{-2}, giving an LDR of 115 dB. The SC device has a linear response from 7.8×10^{-10} W cm^{-2} to 2.1×10^{-3} W cm^{-2}, corresponding to a higher LDR of 129 dB. Insets in the Fig. 2e are the linear fitting results for each device, where the coefficients are 0.32 and 0.42 for BC and SC devices, in agreement with their responsivities at 860 nm ($R_{BC} = 0.32$, $R_{SC} = 0.42$) as demonstrated in Fig. 2a. Response speed is also an important performance of photodetectors for practical applications [1,2,18]. Fig. 2f shows the transient photo-response behavior of devices at –0.1 V, for which the rise time (t_{rise}) is defined as the time gap when the photocurrent rises from 10% to 90% and the fall time (t_{fall}) is

defined as the time gap when the photocurrent drops from 90% to 10%. The BC device shows t_{rise} and t_{fall} of 9.5 μs and 9.6 μs, respectively. The SC device shows t_{rise} and t_{fall} of 4.5 μs and 5.5 μs, respectively, demonstrating quicker on-off switch to the optical signal. The dynamic response of devices at various light modulation frequencies is shown in Figs. S6c,d. The cutoff frequency is defined as the frequency when the output of a detector drops by 3 dB. The SC device shows a cutoff frequency larger than 10^5 Hz, which is relatively high compared with the BC device with cutoff frequency below 10^5 Hz. These results indicate that the SC device shows faster response to a square-wave light signal and is potential to better fit the requirements for practical applications. The related device parameters discussed above are compiled in Table 1.

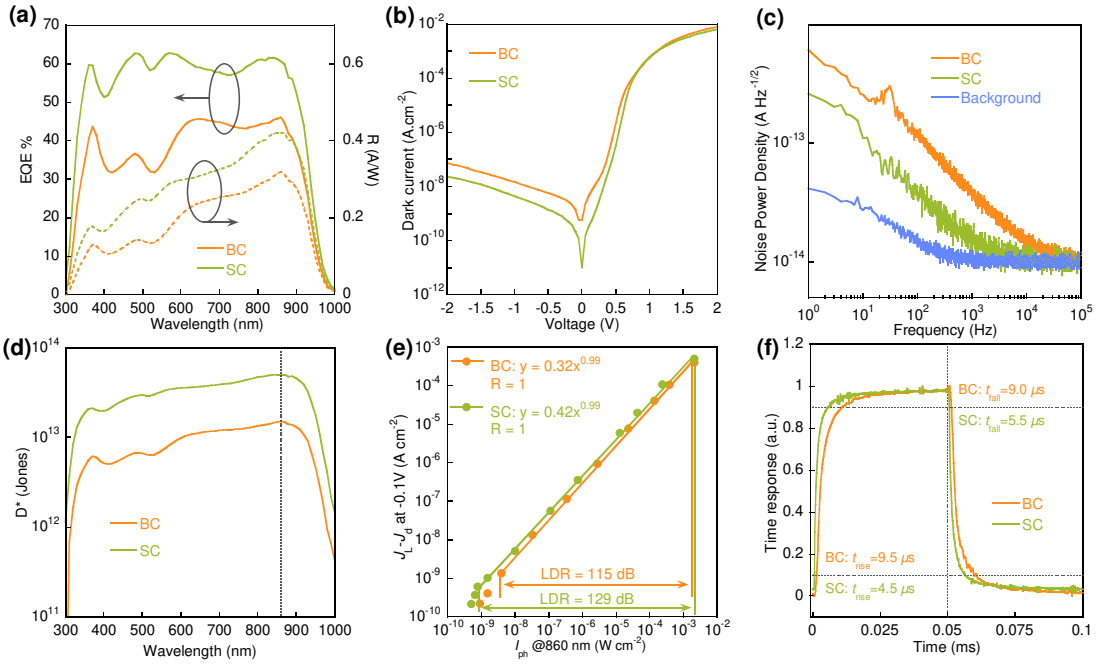

Fig. 2. (a) EQE and responsivity spectra at –0.1 V, (b) dark *J*-*V* curves, (c) noise power spectra, (d) D^* curves derived from EQE and J_d at –0.1 V, (e) LDR and (f) time

response under 10 kHz 860 nm light pulse at –0.1 V of BC and SC devices.

Table 1. OPD performance parameters of BC and SC devices under –0.1 V bias.

Device	J_d (A cm^{-2})	EQE[a] (%)	R^a (A W^{-1})	D^{*b} (Jones)	D^{*c} (Jones)	LDR (dB)	t_{rise} / t_{fall} (μs)
BC	1.4×10^{-9}	46.1	0.32	1.5×10^{13}	4.7×10^{12}	115	9.5 / 9.6
SC	2.2×10^{-10}	60.6	0.42	5.0×10^{13}	9.5×10^{12}	129	4.5 / 5.5

[a] Obtained at 860 nm. [b] Calculated from J_d and EQE at 860 nm. [c] Calculated from noise spectral density at 10 kHz.

2.2 Device physics

The photocurrent density-effective voltage (J_{ph}-V_{eff}) curves of devices are shown in Fig. S7. The photocurrents of both devices increase and reach saturation at high V_{eff} region, where the SC device shows a saturated current density (J_{sat}) of 23.1 mA cm^{-2} at 2 V, higher than the BC device with 19.7 mA cm^{-2}, indicating the increase of overall absorption and exciton generation. The charge collection probabilities (P_c, P_c = J_{ph}/J_{sat}) under short-circuit condition are 66.5% and 78.8% for BC and SC devices, indicating that improved exciton dissociation and charge collection efficiency is obtained by SC device [53]. Transient photovoltage (TPV) and transient photocurrent (TPC) were performed to evaluate charge recombination and charge extraction in devices (Fig. S8) [54,55]. The SC device shows a slower TPV decay time of 104 μs than the BC device with 88 μs, indicative of suppressed charge recombination.

Meanwhile, the SC device presents faster TPC decay time (0.76 μs) compared with the BC device (1.27 μs), signifying improved charge extraction efficiency. The hole (μ_h) and electron (μ_e) mobilities of blend films are evaluated by space-charge-limited current (SCLC) method with charge-only devices (Fig. S9). As shown in Fig. 3a, the SC film shows μ_h and μ_e of 1.8×10^{-4} and 7.9×10^{-4} cm^2 V^{-1} s^{-1}, both of which are higher than those of BC film ($\mu_h = 7.5 \times 10^{-6}$ cm^2 V^{-1} s^{-1}, $\mu_e = 1.1 \times 10^{-4}$ cm^2 V^{-1} s^{-1}). With the *J*-*V* curves of the electron-only devices, the defect states (N_t) were calculated using the equation of $N_t = 2\varepsilon_r\varepsilon_0 \cdot V_{TFL}/qL^2$, where L is the thickness of the active layer and V_{TFL} is the trap-filling limit voltage (Fig. S10) [56]. The V_{TFL} values of BC and SC devices are 0.57 eV and 0.32 eV, corresponding to N_t values of 2.1×10^{15} cm^{-3} and 1.2×10^{15} cm^{-3}, indicating reduced defect states in the SC film. The improved charge generation, transportation, and collection jointly contribute to the EQE increase of the SC device. The improvement of these photophysical processes also implies the decrease of the local defects and impurities that may help to lower the dark current under reverse bias.

The intrinsic origins of dark current in OPDs under reverse bias (saturation current, J_0) were studied. The J_0 consists of a radiative recombination current ($J_{0,R}$) and a non-radiative recombination current ($J_{0,NR}$) [57]. The $J_{0,R}$ is derived from the Fourier transform photocurrent spectroscopy (FTPS) and the absorptivity of blackbody radiation at room temperature, and the $J_{0,NR}$ can be calculated by electroluminescence (EL), as EQE of EL equals to the fraction of $J_{0,R}$ to the sum of $J_{0,R}$ and $J_{0,NR}$ (see the Note 2 and Fig. S11 in supplementary data). The BC device shows a $J_{0,R}$ of 2.8×10^{-18} A cm^{-2} and a $J_{0,NR}$ of 9.5×10^{-13} A cm^{-2}. The SC device shows a $J_{0,R}$ of 1.6×10^{-18} A cm^{-2} and a $J_{0,NR}$ of 3.2×10^{-13} A cm^{-2}. Both $J_{0,R}$ and $J_{0,NR}$ of the SC device are lower than those of the BC device. J_0 is dominated by the $J_{0,NR}$, and the $J_{0,NR}$ of SC is three orders of magnitude lower than the J_d at −0.1 V. Thus, the J_d of the devices is mainly contributed by the extrinsic origins, such as topology defects. The impedance spectra of devices with frequency from 20 Hz to 10 MHz are shown in Fig. 3b. Fitting the curves with circuit model shown in the inset gives the series resistance (R_s) and shunt resistance (R_{sh}) of each device. Both devices

show similar R_s values of ~15 Ω, but the SC device shows an R_{sh} of 451.9 KΩ, significantly higher than the BC device with 298.8 KΩ. According to the equivalent circuit of a photodetector, for a constant current source, lower R_{sh} could share more current flow of the circuit, decreasing the device current (Fig. S12) [58]. Thus, a high R_{sh} is desirable for a photodetector. As R_{sh} is caused by the leakage across the pn-junction due to the defects and impurities in the junction region, the higher R_{sh} in SC device indicates lower leakage current, which is the major origin of the reduced dark current under reverse bias. Shown in Fig. 3c is the density of trap states (tDOS) as a function of energy (tDOS-E_ω) [59], which is deduced from the capacitance-frequency (*C*-*F*) characteristics of devices (Fig. S13). Although the devices have similar peak position of tDOS distribution, the SC device exhibits a diminished profile, suggesting the electron injection under reverse bias is suppressed. Mott-Schottky analysis was performed with capacitance-voltage (*C*-*V*) characteristics of devices (Fig.3d) [60,61], and the *C*-*V* relation can be described by:

$$C^{-2} = \frac{2(V_{bi}-V)}{A^2 q\varepsilon\varepsilon_0 N_A} \quad (4)$$

where A is device area, ε_0 is the vacuum permittivity, ε is the relative permittivity of the blend film (ε ~ 3), V_{bi} is built-in potential, and N_A represents the doping or impurity concentration [62,63]. The N_A values are recorded as 3.6×10^{15} cm^{-3} for the BC device and 2.5×10^{15} cm^{-3} for the SC device, indicating the realization of depressed impurity concentration in SC device. Meanwhile, the lower capacitance peak (0.5-1.1 V in the *C*-*V* curves) of SC device suggests a wider depletion width ($W_{depletion}$) compared with the BC device. The $W_{depletion}$ of each blend film can be derived by

$$W_{depletion} = \sqrt{\frac{2\varepsilon_r\varepsilon_0(V_{bi}-V)}{qN_A}} \quad (5)$$

where *V* is the applied bias [60,62,64,65]. The depletion width as a function of the

applied bias is shown in Fig. S14. At −0.1 V, the $W_{depletion}$ values are 271 nm and 322 nm for BC and SC devices, indicating that the SC devices exhibits a stronger block ability from the reverse injected electrons. Therefore, the impedance spectroscopy, tDOS analysis, and Mott-Schottky analysis demonstrate the suppressed trap states in the SC device, in good agreement with the decreased monomolecular recombination as evaluated by light-intensity dependent open-circuit voltage characteristics (Fig. S15), the less unity deviation of the ideal factor (n) fitted from the dark J-V curves (Fig. S16).

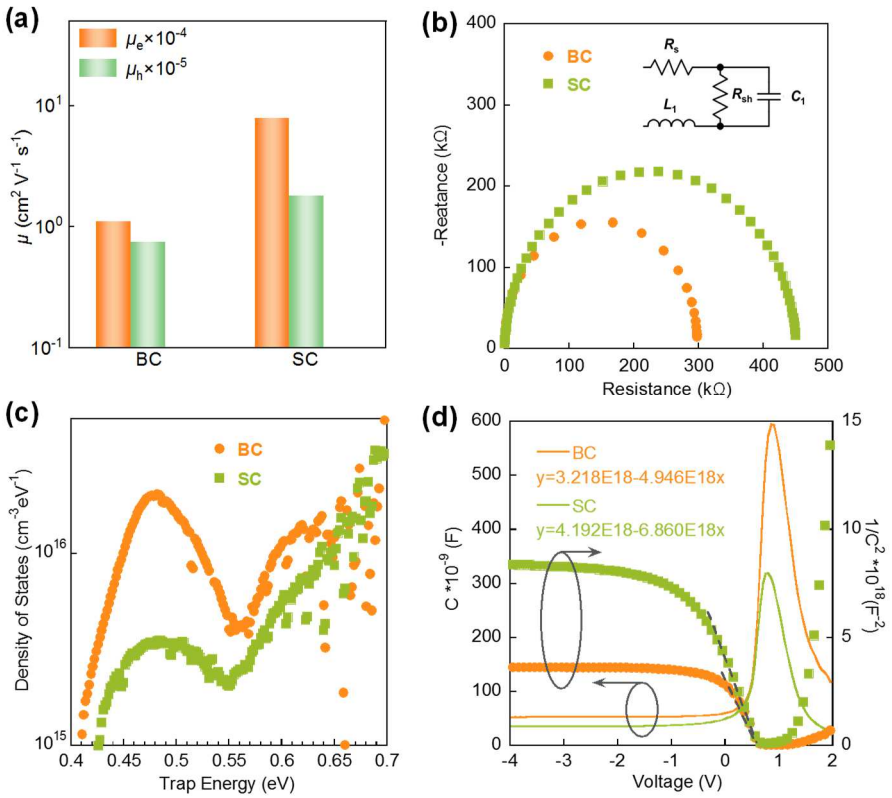

Fig. 3. (a) Summary of hole and electron mobilities of charge-only devices based on BC and SC blend films. (b) Impedance spectra, (c) tDOS as a function of trap energy, (d) C-V and $1/C^2$-V characteristics of BC and SC OPD devices.

2.3 Film morphology

Grazing incidence wide angle x-ray scattering (GIWAXS) was performed to study the crystalline packing in neat and blend films. The incident angle of x-ray was 0.16°, which was used to extract the crystalline information over the film thickness, as indicated by the attenuation length as functions of grazing angle each material at 10 keV (Fig. S17). As shown in Fig. S18, the neat NT812 shows preferential bimodal arrangement consisting of both face-on and edge-on crystalline stacking, with π-π stacking reflection at 1.78 $Å^{-1}$ and lamellar stacking reflection at 0.27 $Å^{-1}$ in both in-plane (IP) and out-of-plane (OOP) directions. The neat IEICO-4F shows intense π-π stacking peak at 1.82 $Å^{-1}$ in the OOP direction and lamellar stacking peak at 0.31 $Å^{-1}$ in the IP direction, indicative of preferential face-on orientation. The appearance of off-axis diffractions at the low-q region (0.3-0.6 $Å^{-1}$ in the q_z direction) indicates the formation of high-quality crystalline packing. The 2D images and sector averaged curves of blend films are shown in Figs. 4a,b, which combine the crystalline signals from both NT812 and IEICO-4F. Multipeak-fitting the IP lamellar reflections can extract the peak area and full width at half maximum (FWHM), which can be used to quantify the crystallinity and crystalline coherence length (CCL, CCL = 2π/FWHM) for each component (Fig. S19). As shown in Fig. 4c, crystallization improvements are seen in the SC film compared with the BC film. The NT812 shows slightly increased crystallinity but decreased CCL compared with the BC film, while the IEICO-4F shows significant enhancement on both crystallinity and CCL, with increase extent of ~55% and ~44%, respectively. Meanwhile, the off-axis spots from IEICO-4F are retained in the SC film, indicating that high-quality IEICO-4F crystallites are

achieved (Fig. S20). It is found that the IEICO-4F shows higher crystallinity and CCLs than those of NT812 in both BC and SC films, which affords more efficient pathways for electron transport. Thus, the electron mobilities are higher than the hole mobilities in both blends, as demonstrated by SCLC measurements. In the SC film, while the crystallization of each material is substantially improved, such improvement of IEICO-4F is more significant, which entails the electron mobility remains higher compared with the hole mobility. Azimuthal analysis for the π-π stacking was done to further investigate the crystalline orientations. As shown in Fig. 4d, the pole figure of the SC film shows narrowed and intensified profile compared with the BC film, suggesting crystallites grow with more preferential face-on arrangements (Fig. S21). Since component concentration varies along the vertical direction of the SC film, the crystalline information near the top surface (~5 nm) was also revealed by GIWAXS with an incident angle of 0.08° (Fig. S22). The comparison of the GIWAXS data probed with 0.08° and 0.16° indicates that the peak area ratio between IEICO-4F and NT812 at the top surface is ~3.2, which is higher than that of ~2.8 in the bulk, indicating the film surface with relatively high IEICO-4F concentration shows more reflection signals associated with IEICO-4F.

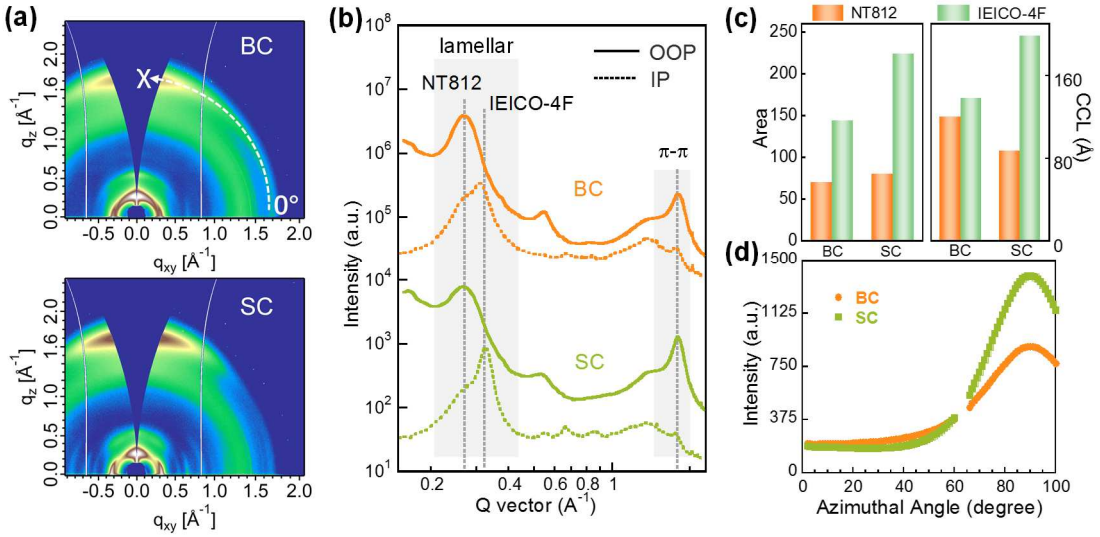

Fig. 4. GIWAXS (a) images and (b) sector averaged curves in the OOP and IP directions of the blend films. (c) Summary of the peak area and CCLs obtained by fitting the lamellar peaks in the IP direction. (d) Pole figure of the π-π stacking of the blend films. The azimuthal angle χ and spreading direction are shown by the dotted arc in the 2D image of the BC film.

The mesoscale morphology in real space was studied by atomic force microscopy (AFM) and transmission electron microscopy (TEM). The AFM height images capture the surface topographic features of the films. As shown in Fig. 5a, fibrillar aggregates appear in the BC film, while the SC film shows homogeneous and poor-defined features. In the TEM images, which are the vertical projections of both the surface and the bulk structures, the BC film shows large-scale aggregates enriched with delicate fibrils (bright region), while the SC film exhibits refined and robust fibril network with tens of nanometers in width (Fig. 5b). Due to the semiflexible backbones, conjugated polymers often crystallize with high aspect ratio by segmental

π-π and lamellar interactions, forming fibril-like crystallites [66-69]. Thus, the fibrillar structures seen in the above images originate from NT812 crystallites. The comparison of AFM and TEM results indicates that the NT812 fibrils in the SC film are mainly presence in the bulk, and delicate and highly aggregated fibrils display over the BC film.

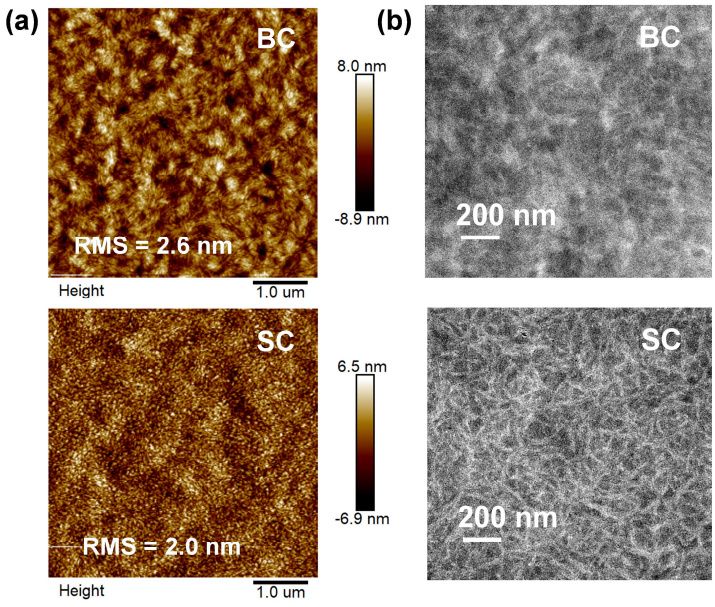

Fig. 5. (a) AFM and (b)TEM images of the blend films.

The length scales of each component in blends were probed by nitrogen K-edge resonant soft x-ray scattering (NK-RSoXS), which is a powerful characterization tool developed for decoupling the multiphase structures in soft matters [70]. As shown in Fig. 6a, the neat NT812 and IEICO-4F show distinct near edge x-ray absorption fine structure (NEXAFS) signatures at 399 eV and 400 eV, which arise from N 1s→π* transitions localized within the benzothiadiazole units of NT812 and the cyano-groups of IEICO-4F, respectively [70]. The NEXAFS spectra determine the absorptive

component β of complex indexes of refraction, and the dispersive component δ can be calculated by β via Kramer-Kronigs relationship (Fig. 6b) [71], enabling the calculation of contrast function $\Delta\delta^2 + \Delta\beta^2$ between NT812 and IEICO-4F (Fig. 6c). It can be seen that the refractive indexes of NT812 and IEICO-4F show substantial changes when the x-ray energy is approaching 399 eV and 400 eV, respectively, leading to intense compositional contrast with chemical specificity. Thus, NK-RSoXS of blend films was performed to resolve the phase separation contributed by NT812 at 399 eV and IEICO-4F at 400 eV. The RSoXS averaged *I*-*q* curves are shown in Figs. 6d,e, where strong resonant signals present at 399 eV and 400 eV in comparison with those recorded at the pre-edge energy (395 eV) and the post-edge energy (406 eV), in good agreement with the calculated contrast function. The peak positions in the *I*-*q* curves were determined by fitting their corresponding Iq^2-*q* curves (Figs. S23 and S24). The BC film shows broad scattering interferences at ~0.0043 $Å^{-1}$ under 399 eV and ~0.0038 $Å^{-1}$ under 400 eV, corresponding to characteristic distances of 147 nm and 164 nm, respectively. The SC film shows scattering humps at ~0.011 $Å^{-1}$ under 399 eV and ~0.0091 $Å^{-1}$ under 400 eV, corresponding to characteristic distances of 55 nm and 69 nm, respectively. The combination of the NK-RSoXS and AFM/TEM images unlocks the multiphase structures in blend films. In the BC film, the large domain distance of NT812 is likely stemming from the correlations between the fibrillar aggregates, while the IECIO-4F is of low crystallinity and sparsely distributes among the aggregates. The fibrils within the aggregates may also have inter-distance, but the scattering interference does not appear in the high-*q* region of the *I*-*q* curve at

399 eV, which may be due to the weak intensity. In the SC case, the NT812 is refined into robust fibrillar network with an inter-fibril space of 55 nm, and the enhanced IEICO-4F crystallization leads to decreased inter-crystallite distance of 69 nm. Fig. 6f schematically shows the phase-separated morphology of BC and SC films based on the scattering and microscopy results, where the multiple phases are demonstrated, including the NT812 crystalline fibrils, IEICO-4F crystalline domains, and the amorphous mixing region. Such phases are inter-connected with complex domain interfaces, and show collective behaviors affording optoelectronic performances [72-74].

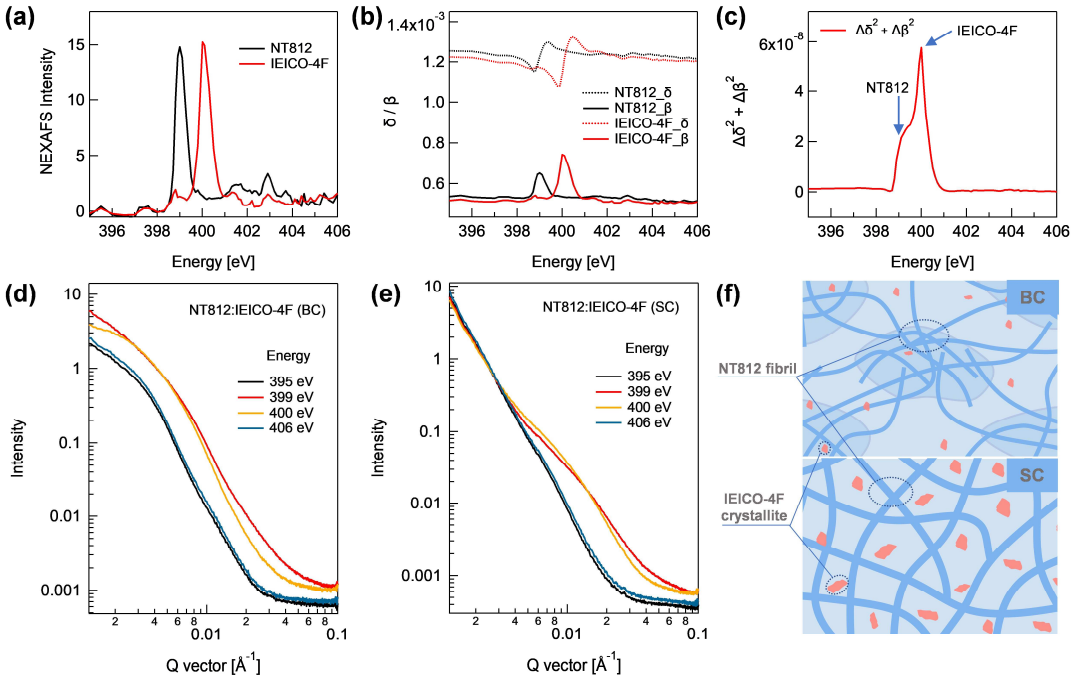

Fig. 6. (a) Normalized NEXFAS spectra and (b) complex indexes of refraction of neat materials. The NEXAFS spectra were collected with total electron yield (TEY) mode. (c) Calculated contrast function between NT812 and IEICO-4F at N K-edge. NK-RSoXS *I*-*q* curves of (d) BC and (e) SC films at various energies. (f) Schematic

representations of multiphase morphology of BC and SC films. The light-blue background represents the amorphous mixing comprising both NT812 and IEICO-4F.

Therefore, the results reveal the fundamental advantages of SC on morphology and the impacts on the OPD performance. IEICO-4F was well dissolved in CF without heterogeneous interactions from NT812, which provided a favorable crystallization environment during drying. Thus, high-quality IEICO-4F crystallites with more preferential face-on orientation were obtained. Unlike blend casting, the pre-deposited NT812 layer was re-dissolved by CF when the IEICO-4F was casted atop. The re-dissolution was insufficient, as the processes including dissolution and drying were terminated within seconds, which highly increased the viscosity of NT812 chains that rapidly crystallized in the form of fibrillar network [75]. Such refined and robust NT812 fibrils laid the foundation of phase-separated framework, in-between which the IEICO-4F crystallites infiltrated from the top to the bottom. Although cross-section scanning electron microscopy (SEM) cannot defined the phase separation from each material in the vertical direction (Fig. S25), the surface and bulk information resulted from AFM, TEM, and NK-RSoXS, coupled with a ~300 nm thickness that covers the characteristic lengths of phase separation, can be used to appropriately describe the vertical morphology for both blends as schematically shown in Fig. 7a. The combination of high-quality IEICO-4F crystallites and refined NT812 fibrillar network suppresses the local defects and imperfections, offering efficient transport channels for both electrons and holes. The NT812 fibrils are not

independent of the multiphase system, since the polymer crystallites are formed by chain-segmental packing, leaving other segments to participate into the mixing region, which can efficiently extract the generated charges at the D/A interface [76]. Thus, charge generation, transportation and collection are significantly improved, boosting the EQE and response speed of the SC device. The gradient multiphase distribution in vertical direction effectively diminishes the trap states in the SC film, as well as the dark/noise current under reverse bias of the SC device (Fig. 7b). Therefore, the simultaneous achievement of high EQE and low dark/noise current enables significantly improved OPD performances of the SC film.

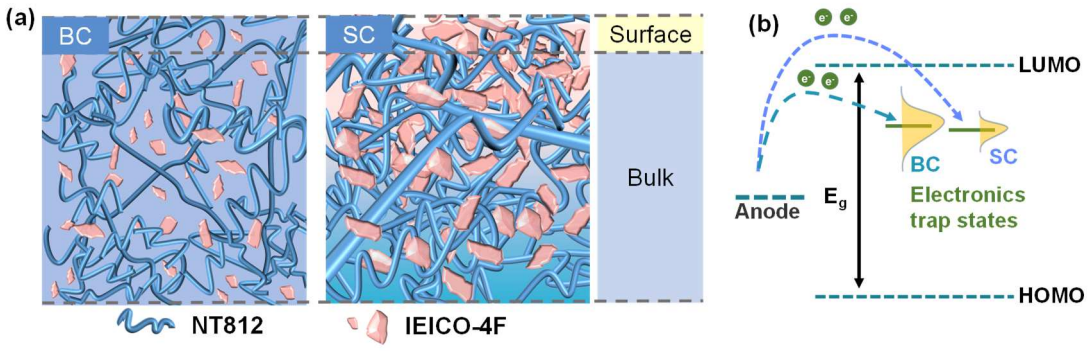

Fig. 7. (a) Schematic representations of multiphase morphology in vertical direction of BC and SC films. The light-blue background stands for the mixing matrix comprising amorphous NT812 and IEICO-4F. (b) Suppressed tDOSs in the SC film that assists in reducing the device dark current under reverse bias.

2.4 Effectiveness of refined fibrillar multiphase morphology

To study the advantages of the refined fibrillar multiphase morphology on other blend

systems, NT812:COTIC-4F and NT812:Y6 were used to fabricate the OPD devices by BC and SC, respectively. The chemical structures of COTIC-4F and Y6 are shown in Fig. S26a. The TEM images of blends, dark *J*-*V* characteristics and D^* curves of devices are summarized in Fig. 8. Device EQE and R spectra at –0.1 V are shown in Figs. S26 b,c. For the NT812:COTIC-4F case, similar refined and robust NT812 fibril network is seen in the SC film, corresponding to reduced dark current at reverse bias and increased detectivities compared with the BC film. The maximum D^* appears at 1050 nm over 5.0×10^{12} Jones, which is a high OPD detectivity with response wavelength longer than 1000 nm [29,34,40,46]. For the NT812:Y6 case, the TEM image of BC film shows high contrast between the bright and dark regions, where the bright region is enriched with fibrillar structures, indicative of large-scale aggregates. A refined and uniform fibril network is seen in the SC film, which drastically decreases device dark/noise current by two orders of magnitude lower than the SC device. Such decrease is huge in comparison with NT812:IEICO-4F and NT812:Y6 blends, and a maximum D^* is obtained at ~860 nm over 1.3×10^{13} Jones, which is one order magnitude higher than that of the BC devices. These results demonstrate the effectiveness of the refined fibril-based multiphase morphology, which is potential to provide guidelines for structural manipulation in various OPD blend systems.

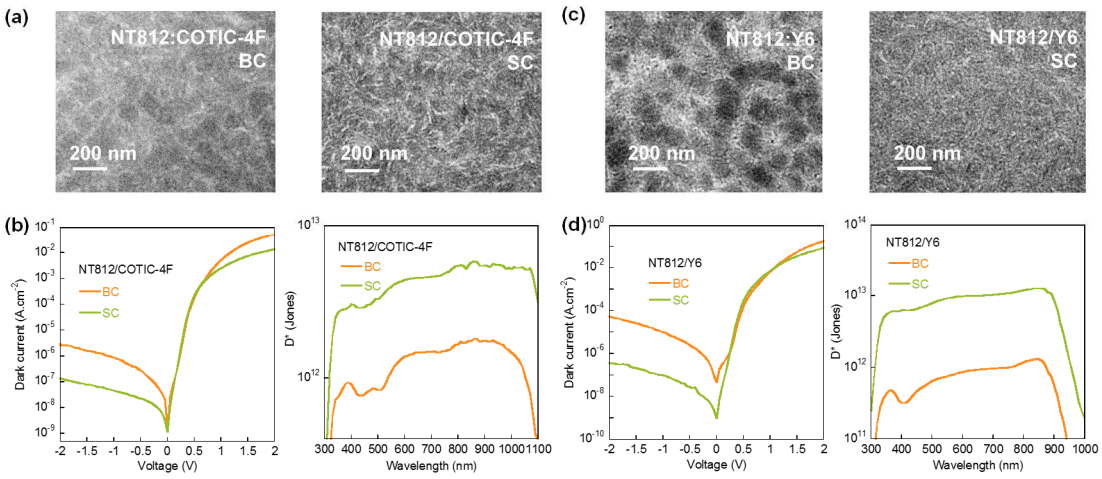

Fig. 8. (a) TEM images and (b) device dark *J-V* and D^* curves of NT812:COTIC-4F blends. (c) TEM images and (d) device dark *J-V* and D^* curves of NT812:Y6 blends.

3. Conclusion

The utilization of SC for active-layer processing successfully demonstrates highly enhanced NT812:IEICO-4F based OPD performances, with highest D^* of 5.0×10^{13} Jones at 860 nm under –0.1 V and improved LDR and response speed, indicating the strong vis-to-NIR sensing capability and potential for practical applications. SC leads to the formation of a refined fibrillar multiphase morphology, where from the surface to the bulk, high-quality IEICO-4F crystallites infiltrate the robust NT812 fibrils. Such morphology improvements lead to enhanced charge generation and transportation, reduced trap states, and strong block ability to reverse electron injection, substantially increasing the EQE and decreasing the dark/noise current. Similar performance enhancements are seen from OPD devices based on NT812:COTIC-4F and NT812:Y6 blends, indicating that the SC-induced refined

fibrillar multiphase morphology can bring new opportunities for developing high-performance OPDs.

Declaration of Competing Interest

The authors declare that they have no known competing financial interests or personal relationships that could have appeared to influence the work reported in this paper.

Acknowledgements:

W. Z. was supported by National Natural Science Foundation of China (Grant No. 22109094) and the fellowship of China Postdoctoral Science Foundation (No. 2022M712054). GIWAXS and RSoXS/NEXAFS were performed at beamlines 7.3.3 and 11.0.1.2 at the Advanced Light Source, a U.S. DOE Office of Science User Facility under contract no. DE-AC02-05CH11231.

References

[1] H. Bin, T. P.A. van der Pol, J. Li, B. T.van Gorkom, M. M. Wienk, R. A. J. Janssen, Efficient organic solar cells with small energy losses based on a wide-bandgap trialkylsilyl-substituted donor polymer and a non-fullerene acceptor, Chem. Eng. J. 435 (2022) 134878.

[2] C. Wang, X. Zhang, W. Hu, Organic photodiodes and phototransistors toward infrared detection: materials, devices, and applications, Chem. Soc. Rev. 49 (2020) 653-670.

[3] C. Fuentes-Hernandez, W. F. Chou, T. M. Khan, L. Diniz, J. Lukens, F. A. Larrain, V. A. Rodriguez-Toro and B. Kippelen, Large-area low-noise flexible organic photodiodes for detecting faint visible light, Science, 370. 6517 (2020) 698-701.

[4] K. D. Hakkel, M. Petruzzella, F. Ou, A. van Klinken, F. Pagliano, T. Liu, R. P. J. van Veldhoven, A. Fiore, Integrated near-infrared spectral sensing, Nat.

Commun. 13 (2022) 1-8.

[5] P. C. Y. Chow, T. Someya, Organic photodetectors for next-generation wearable electronics, Adv. Mater. 32 (2020) 1902045.

[6] Z. Lan, Y. Lei, E. Chan Wing Kin, S. Chen, D. Luo, F. Zhu, Near-infrared and visible light dual-mode organic photodetectors, Sci. Adv. 6 (2021) eaaw8065.

[7] M. Liu, J. Wang, Z. Zhao, K. Yang, P. Durand, F. Ceugniet, G. Ulrich, L. Niu, Y. Ma, N. Leclerc, X. Ma, L. Shen, F. Zhang, Ultra-narrow-band NIR photomultiplication organic photodetectors based on charge injection narrowing, J. Phys. Chem. Lett. 12. 11 (2021) 2937-2943.

[8] Y. Zheng, Y. Chen, Y. Cao, F. Huang, Y. Guo, X. Zhu, Design of all-fused-ring nonfullerene acceptor for highly sensitive self-powered near-infrared organic photodetectors, ACS Materials Lett. 4 (2022) 882-890.

[9] Y. Chen, Y. Zheng, Y. Jiang, H. Fan, X. Zhu, Carbon-bridged 1,2-bis(2-thienyl)ethylene: an extremely electron rich dithiophene building block enabling electron acceptors with absorption above 1000 nm for highly sensitive NIR photodetectors, Am. Chem. Soc. 143. 11 (2021) 4281-4289.

[10] Q. Li, Y. Guo, Y. Liu, Exploration of near-infrared organic photodetectors. Chem. Mater. 31 (2019) 6359-6379.

[11] S. Xing, V. C. Nikolis, J. Kublitski, E. Guo, X. Jia, Y. Wang, D. Spoltore, K. Vandewal, H. Kleemann, J. Benduhn, K. Leo, Miniaturized VIS-NIR spectrometers based on narrowband and tunable transmission cavity organic photodetectors with ultrahigh specific detectivity above 10^{14} Jones. Adv. Mater. 33 (2021), 2102967.

[12] H. J. Eun, H. Kye, D. Kim, I. S. Jin, J. W. Jung, S.-J. Ko, J. Heo, B.-G. Kim, J. H. Kim, Effective dark current suppression for high-detectivity organic near-infrared photodetectors using a non-fullerene acceptor, ACS Appl. Mater. Interfaces 13 (2021) 11144-11150.

[13] W. Liu, S. Sun, S. Xu, H. Zhang, Y. Zheng, Z. Wei, X. Zhu, Theory-guided material design enabling high-performance multifunctional semitransparent organic photovoltaics without optical modulations, Adv. Mater. 34 (2022) 2200337.

[14] Z. Xiao, X. Jia, L. Ding, Ternary organic solar cells offer 14% power conversion efficiency, Sci. Bull, 62. 23 (2017) 1562-1564.

[15] Z. Liu, T-K. Lau, G. Zhou, S. Li, J. Ren, S. K. Das, R. Xia, G. Wu, H. Zhu, X.

Lu, H-L. Yip, H. Chen, C. Li, Achieving efficient organic solar cells and broadband photodetectors via simple compositional tuning of ternary blends, Nano Energy 63 (2019) 103807.

[16] W. Liu, S. Sun, L. Zhou, Y. Cui, W. Zhang, J. Hou, F. Liu, S. Xu, X. Zhu, Design of near-infrared nonfullerene acceptor with ultralow nonradiative voltage loss for high-performance semitransparent ternary organic solar cells, Angew. Chem. Int. Ed. 61 (2022), e202116111.

[17] L. Meng, Y. Zhang, X. Wan, L. Ding, Organic and solution-processed tandem solar cells with 17.3% efficiency, Science, 361. 6407 (2018) 1094-1098.

[18] J. Huang, J. Lee, J. Vollbrecht, V. V. Brus, A. L. Dixon, D. X. Cao, Z. Zhu, Z. Du, H. Wang, K. Cho, G. C. Bazan, T.-Q. Nguyen, A high-performance solution-processed organic photodetector for near-infrared sensing, Adv. Mater. 32 (2020), 1906027.

[19] Y. Liu, M. Zhu, J. Sun, W. Shi, Z. Zhao, X. Wei, X. Huang, Y. Guo, Y. Liu, A self-assembled 3D penetrating nanonetwork for high-performance intrinsically stretchable polymer light-emitting diodes, Adv. Mater. (2022), 202201844.

[20] K. Jiang, J. Zhang, Z. Peng, F. Lin, S. Wu, Z. Li, Y. Chen, H. Yan, H. Ade, Z. Zhu, A. K.-Y. Jen, Pseudo-bilayer architecture enables high-performance organic solar cells with enhanced exciton diffusion length, Nat. Commun. 12. 1 (2021) 1-9.

[21] J. Yuan, Y. Zhang, L. Zhou, G. Zhang, H.-L. Yip, T.-K. Lau, X. Lu, C. Zhu, H. Peng, P. A. Johnson, M. Leclerc, Y. Cao, J. Ulanski, Y. Li, Y. Zou, Single-Junction organic solar cell with over 15% efficiency using fused-ring acceptor with electron-deficient core, Joule 3 (2019) 1140-1151.

[22] Z. Zhao, C. Li, L. Shen, X. Zhang, F. Zhang, Photomultiplication type organic photodetectors based on electron tunneling injection, Nanoscale 12 (2020) 1091-1099.

[23] J. Wang, S.-C. Chen, Z. Yin, Q. Zheng, Broadband organic photodetectors based on ternary blend active layers with enhanced and spectrally flat response, J. Mater. Chem. C 8 (2020) 14049-14055.

[24] Z. Zhong, F. Peng, Z. Huang, L. Ying, G. Yu, F. Huang, Y. Cao, High-detectivity non-fullerene organic photodetectors enabled by a cross-linkable electron blocking layer, ACS Appl. Mater. Interfaces 12 (2020) 45092-45100.

[25] Z. Huang, Z. Zhong, F. Peng, L. Ying, G. Yu, F. Huang, Y. Cao, Copper thiocyanate as an anode interfacial layer for efficient near-infrared organic

photodetector, ACS Appl. Mater. Interfaces 13 (2021) 1027-1034.

[26] Y. Wei, H. Chen, T. Liu, S. Wang, Y. Jiang, Y. Song, J. Zhang, X. Zhang, G. Lu, F. Huang, Z. Wei, H. Huang, Self-powered organic photodetectors with high detectivity for near infrared light detection enabled by dark current reduction, Adv. Funct. Mater. 31 (2021) 2106326.

[27] J. C. Ho, A. Arango, V. Bulović, Lateral organic bilayer heterojunction photoconductors, Appl. Phys. Lett. 93 (2008) 063305.

[28] H. Ning, Q. Jiang, P. Han, M. Lin, G. Zhang, J. Chen, H. Chen, S. Zeng, J. Gao, J. Liu, F. He, Q. Wu, Manipulating the solubility properties of polymer donors for high-performance layer-by-layer processed organic solar cells, Energy Environ. Sci, 14. 11 (2021) 5919-5928.

[29] Z. Zhong, L. Bu, P. Zhu, T. Xiao, B. Fan, L. Ying, G. Lu, G. Yu, F. Huang, Y. Cao, Dark current reduction strategy via a layer-by-layer solution process for a high-performance all-polymer photodetector, ACS Appl. Mater. Interfaces, 11 (2019) 8350-8356.

[30] K. Weng, L. Ye, L. Zhu, J. Xu, J. Zhou, X. Feng, G. Lu, S. Tan, F. Liu, Y. Sun, Optimized active layer morphology toward efficient and polymer batch insensitive organic solar cells, Nat. Comm. 11 (2020) 2855.

[31] Y. Zhang, B. Wu, Y. He, W. Deng, J. Li, N. Qiao, Y. Xing, X. Yuan, N. Li, C. J. Brabec, H. Wu, G. Lu, C. Duan, F. Huang, Y. Cao, Achieving efficient organic solar cells and broadband photodetectors via simple compositional tuning of ternary blends, 93 (2022) 106858.

[32] Y. Xu, J. Yuan, S. Liang, J.-D. Chen, Y. Xia, B. W. Larson, Y. Wang, G. M. Su, Y. Zhang, C. Cui, M. Wang, H. Zhao, W. Ma, Simultaneously improved efficiency and stability in all-polymer solar cells by a P–i–N architecture, ACS Energy Lett. 4 (2019) 2277-2286.

[33] Y. Yue, B. Zheng, W. Yang, L. Huo, J. Wang, L. Jiang, Meniscus-assisted coating with optimized active-layer morphology toward highly efficient all-polymer solar cells, Adv. Mater. (2022) 2108508.

[34] J. Lee, S. Ko, H. Lee, J. Huang, Z. Zhu, M. Seifrid, J. Vollbrecht, V. V. Brus, A. Karki, H. Wang, K. Cho, T. Nguyen, G. C. Bazan, Side-chain engineering of nonfullerene acceptors for near-infrared organic photodetectors and photovoltaics, ACS Energy Lett. 4 (2019) 1401-1409.

[35] Z. S. Parr, J. B. -González, R. B. Rashid, K. J. Thorley, D. Meli, B. D. Paulsen, J.

Strzalka, J. Rivnay, C. B. Nielsen, From p- to n-type mixed conduction in isoindigo-based polymers through molecular design, Adv. Mater. (2022) 2107829.

[36] Y. Xia, L. E. Aguirre, X. Xu, O. Inganäs, All-polymer high-performance photodetector through lamination, Adv. Electron. Mater. (2020) 1901017.

[37] K. Yang, J. Wang, Z. Zhao, Y. Sun, M. Liu, Z. Zhou, X. Zhang, F. Zhang, Highly sensitive photomultiplication type polymer photodetectors by manipulating interfacial trapped electron density, Chem. Eng. J. 435 (2022) 134973.

[38] C. Xu, P. Liu, C. Feng, Z. He, Y. Cao, Organic photodetectors with high detectivity for broadband detection covering UV-vis-NIR, J Mater. Chem. C 10. 15 (2022) 5787-5796.

[39] X. Wei, H. Gao, J. Feng, Y. Pi, B. Zhang, Y. Zhai, W. Wen, M. He, J. R. Matthews, H. Wang, Y. Li, S. Jiang, L. Jiang, Y. Wu, Highly ordered semiconducting polymer arrays for sensitive photodetectors, ACS Appl. Mater. Interfaces 11 (2019) 15829-15836.

[40] J. Lee, S. Ko, M. Seifrid, H. Lee, B. R. Luginbuhl, A. Karki, M. Ford, K. Rosenthal, K. Cho, T. Nguyen, G. C. Bazan, Bandgap narrowing in non-fullerene acceptors: single atom substitution leads to high optoelectronic response beyond 1000 nm, Adv. Energy Mater. 8 (2018) 1801212.

[41] N. Gasparini, A. Gregori, M. Salvador, M. Biele, A. Wadsworth, S. Tedde, D. Baran, I. McCulloch, C. J. Brabec, Visible and near-infrared imaging with nonfullerene-based photodetectors, Adv. Mater. Technol. 3 (2018) 1800104.

[42] Z. Zhong, K. Li, J. Zhang, L. Ying, R. Xie, G. Yu, F. Huang, Y. Cao, High-performance all-polymer photodetectors via a thick photoactive layer strategy. ACS Appl. Mater. Interfaces 11 (2019) 14208.

[43] W. Li, Y. Xu, X. Meng, Z. Xiao, R. Li, L. Jiang, L. Cui, M. Zheng, C. Liu, L. Ding, Q. Lin, Visible to near-infrared photodetection based on ternary organic heterojunctions, Adv. Funct. Mater. (2019) 1808948.

[44] K. Yang, J. Wang, J. Miao, J. Zhang, F. Zhang, All-polymer photodetectors with photomultiplication, J. Mater. Chem. C, 7 (2019) 9633-9640.

[45] Z. Zhao, J. Wang, C. Xu, K. Yang, F. Zhao, K. Wang, X. Zhang, F. Zhang, Photomultiplication type broad response organic photodetectors with one absorber layer and one multiplication layer, J. Phys. Chem. Lett. 11 (2020) 366-373.

[46] Z. Zhong, F. Peng, L. Ying, G. Yu, F. Huang, Y. Cao, Ternary organic photodiodes with spectral response from 300 to 1200 nm for spectrometer application, Sci China Mater, 64. 10 (2021) 2430-2438.

[47] W. Ren, Q. Tan, Q. Wang, Y. Liu, Hybrid organolead halide perovskite microwire arrays/single CdSe nanobelt for a high-performance photodetector, Chem. Eng. J. 406 (2021) 126779.

[48] Y. Yue, M. Li, H. Li, N. Chai, Y. Dong, Z. Li, X. Chen, X. Wang, One-step anti-solvent associated method for high performance two-dimensional perovskite photodetectors fabrication at low temperature, Chem. Eng. J. 444 (2022) 135997.

[49] K. Yang, Z. Zhao, M. Liu, Z. Zhou, K. Wang, X. Ma, J. Wang, Z. He, F. Zhang, Employing liquid crystal material as regulator to enhance performance of photomultiplication type polymer photodetectors, Chem. Eng. J. 427 (2022) 131802.

[50] M. Biele, C. Montenegro Benavides, J. Hürdler, S. F. Tedde, C. J. Brabec, O. Schmidt, Spray-coated organic photodetectors and image sensors with silicon-like performance, Adv. Mater. Technol. 4 (2019) 1800158.

[51] S. Xiong, J. Li, J. Peng, X. Dong, F. Qin, W. Wang, L. Sun, Y. Xu, Q. Lin, Y. Zhou, Water transfer printing of multilayered near-infrared organic photodetectors, Adv. Optical Mater. (2021) 2101837.

[52] B. Park, J. Jung, D. Lim, H. Lee, S. Park, M. Kyeong, S. Ko, S. Eom, S. Lee, C. Lee, S. Yoon, Significant dark current suppression in organic photodetectors using side chain fluorination of conjugated polymer, Adv. Funct. Mater. (2021) 2108026.

[53] W. Zhong, J. Cui, B. Fan, L. Ying, Y. Wang, X. Wang, G. Zhang, X. -F. Jiang, F. Huang, Y. Cao, Enhanced photovoltaic performance of ternary polymer solar cells by incorporation of a narrow-bandgap nonfullerene acceptor, Chem. Mater. 29. 19 (2017) 8177-8189.

[54] K.-H. Kuo, R. Estrada, C.-C. Lee, N.R. Al Amin, Y.-Z. Li, M.Y. Hadiyanto, S.-W. Liu, K.-T. Wong, A new dioxasilepine–aryldiamine hybrid electron-blocking material for wide linear dynamic range and fast response organic photodetector, ACS Appl. Mater. Interfaces 14 (2022) 18782-18793.

[55] V. Roiati, S. Colella, G. Lerario, L. De Marco, A. Rizzo, A. Listorti, G. Gigli, Investigating charge dynamics in halide perovskite-sensitized mesostructured solar cells, Energy Environ. Sci. 7 (2014) 1889-1894.

[56] D. Shi, V. Adinolfi, R. Comin, M. Yuan, E. Alarousu, A. Buin, Y. Chen, S. Hoogland, A. Rothenberger, K. Katsiev, Y. Losovyj, X. Zhang, P.A. Dowben, O.F. Mohammed, E.H. Sargent, O.M. Bakr, Low trap-state density and long carrier diffusion in organolead trihalide perovskite single crystals, Science 347 (2015) 519-522.

[57] J. Li, G. Liu, W. Liu, Y. Si, W. Deng, H. Wu, Highly sensitive uv–vis-to-near-infrared organic photodetectors employing ZnO: polyethylenimine ethoxylated composite as hole-blocking layer, Adv. Photonics Res. 3 (2022) 2100269.

[58] D. Yang, D. Ma, Development of Organic Semiconductor Photodetectors: From Mechanism to Applications, Adv. Opt. Mater. 7 (2019) 1800522.

[59] J. Kublitski, A. Hofacker, B. K. Boroujeni, J. Benduhn, V. C. Nikolis, C. Kaiser, D. Spoltore, H. Kleemann, A. Fischer, F. Ellinger, K. Vandewal, K. Leo, Reverse dark current in organic photodetectors and the major role of traps as source of noise, Nat. Commun. 12 (2021) 1-9.

[60] H. Aqoma, M. Mubarok, W. Hadmojo, E. Lee, T. Kim, T. Ahn, S. Oh, S. Jang, High-efficiency photovoltaic devices using trap-controlled quantum-dot ink prepared via phase-transfer exchange, Adv. Mater. 29 (2017) 1605756.

[61] W. Yao, Z. Wu, E. Huang, L. Huang, A. E. London, Z. Liu, J. D. Azoulay, T. N. Ng, Organic bulk heterojunction infrared photodiodes for imaging out to 1300 nm, ACS Appl. Electron. Mater. 1 (2019) 660-666.

[62] T. Kirchartz, W. Gong, S. A. Hawks, T. Agostinelli, R. C. I. MacKenzie, Y. Yang, J. Nelson, Sensitivity of the Mott–Schottky analysis in organic solar cells, J. Phys. Chem. C 116 (2012) 7672-7680.

[63] B. Xiao, M. Zhang, J. Yan, G. Luo, K. Gao, J. Liu, Q. You, H.-B. Wang, C. Gao, B. Zhao, X. Zhao, H. Wu, F. Liu, High efficiency organic solar cells based on amorphous electron-donating polymer and modified fullerene acceptor, Nano Energy 39 (2017) 478-488.

[64] X. Zhang, J. Zhang, D. Phuyal, J. Du, L. Tian, V. A. Öberg, M. B. Johansson, U. B. Cappel, O. Karis, J. Liu, H. Rensmo, G. Boschloo, E. M. Johansson, Inorganic CsPbI3 perovskite coating on PbS quantum dot for highly efficient and stable infrared light converting solar cells, Adv. Energy Mater. 8 (2018) 1702049.

[65] I. Zonno, A. Martinez-Otero, J. Hebig, T. Kirchartz, Understanding mott-schottky measurements under illumination in organic bulk heterojunction solar cells, Phys. Rev. Appl. 7 (2017) 034018.

[66] R.J. Kline, M.D. McGehee, E.N. Kadnikova, J. Liu, J.M.J. Fréchet, M.F. Toney, Dependence of regioregular poly (3-hexylthiophene) film morphology and field-effect mobility on molecular weight, Macromolecules 38 (2005) 3312-3319.

[67] S. Wang, M. Kappl, I. Liebewirth, M. Müller, K. Kirchhoff, W. Pisula, K. Müllen, Organic field-effect transistors based on highly ordered single polymer fibers, Adv. Mater. 24 (2012) 417-420.

[68] F. Liu, C. Wang, J.K. Baral, L. Zhang, J.J. Watkins, A.L. Briseno, T.P. Russell, Relating chemical structure to device performance via morphology control in diketopyrrolopyrrole-based low band gap polymers, J. Am. Chem. Soc. 135 (2013) 19248-19259.

[69] W. Li, K.H. Hendriks, A. Furlan, W.S.C. Roelofs, M.M. Wienk, R.A.J. Janssen, Universal correlation between fibril width and quantum efficiency in diketopyrrolopyrrole-based polymer solar cells, J. Am. Chem. Soc. 135 (2013) 18942-18948.

[70] W. Zhong, M. Zhang, G. Freychet, G.M. Su, L. Ying, F. Huang, Y. Cao, Y. Zhang, C. Wang, F. Liu, Decoupling Complex Multi-Length-Scale Morphology in Non-Fullerene Photovoltaics with Nitrogen K-Edge Resonant Soft X-ray Scattering, Adv. Mater. 34 (2022) 2107316.

[71] B. Watts, Calculation of the Kramers-Kronig transform of X-ray spectra by a piecewise Laurent polynomial method, Opt. Express 22 (2014) 23628-23639.

[72] J.R. Tumbleston, B.A. Collins, L. Yang, A.C. Stuart, E. Gann, W. Ma, W. You, H. Ade, The influence of molecular orientation on organic bulk heterojunction solar cells, Nat. Photonics 8 (2014) 385-391.

[73] T. Hao, W. Zhong, S. Leng, R. Zeng, M. Zhang, L. Zhu, Y. Yang, J. Song, J. Xu, G. Zhou, Y. Zou, Y. Zhang, F. Liu, The structure-performance correlation of bulk-heterojunction organic solar cells with multi-length-scale morphology, Sci. China Chem. 65 (2022) 1634-1641.

[74] J. Song, M. Zhang, T. Hao, J. Yan, L. Zhu, G. Zhou, R. Zeng, W. Zhong, J. Xu, Z. Zhou, X. Xue, C.-C. Chen, W. Tang, H. Zhu, Z. Ma, Z. Tang, Y. Zhang, F. Liu, Design rules of the mixing phase and impacts on device performance in high-efficiency organic photovoltaics, Research 2022 (2022) 9817267.

[75] J.J. van Franeker, M. Turbiez, W. Li, M.M. Wienk, R.A.J. Janssen, A real-time study of the benefits of co-solvents in polymer solar cell processing, Nat. Comm. 6 (2015) 6229.

[76] L. Zhu, W. Zhong, C. Qiu, B. Lyu, Z. Zhou, M. Zhang, J. Song, J. Xu, J. Wang, J. Ali, W. Feng, Z. Shi, X. Gu, L. Ying, Y. Zhang, F. Liu, Aggregation-induced multilength scaled morphology enabling 11.76% efficiency in all-polymer solar cells using printing fabrication, Adv. Mater. 31 (2019) 1902899.

Graphic Abstract

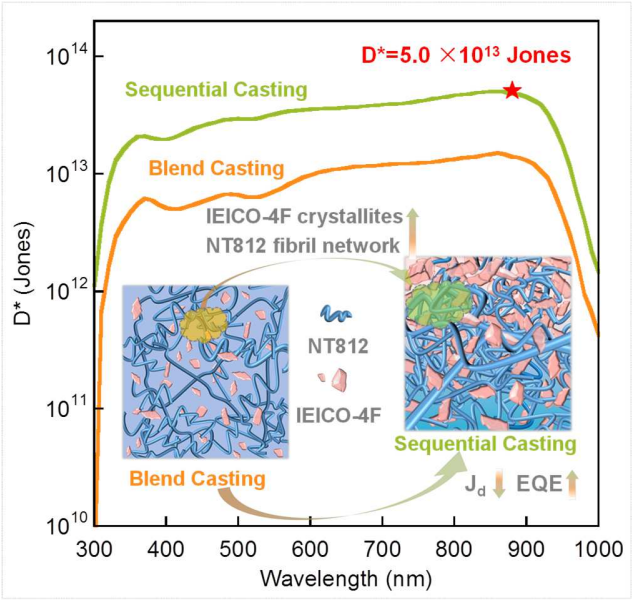

A refined fibrillar multiphase thin-film morphology for organic photodetectors is demonstrated by sequential casting, where from the surface to the bulk, high-quality acceptor crystallites infiltrate the donor fibril network, enabling substantial optimization of device performances.